Improved Electro- and Photocatalytic Water Reduction by Confined Cobalt Catalysts in Streptavidin

Arnau Call,[†,‡] Carla Casadevall,[†,‡] Adrian Romero-Rivera,[§] Vlad Martin-Diaconescu,[†] Dayn J. Sommer,[∥] Sílvia Osuna,[§,⊥] Giovanna Ghirlanda,[*,∥] and Julio Lloret-Fillol[*,†,⊥]

[†]Institute of Chemical Research of Catalonia (ICIQ), The Barcelona Institute of Science and Technology, Avinguda Països Catalans 16, 43007 Tarragona, Spain

[§]Institut de Química Computacional i Catàlisi (IQCC) and Departament de Química, Universitat de Girona, Carrer Maria Aurèlia Capmany 69, 17003 Girona, Spain

[∥]School of Molecular Sciences, Arizona State University, Tempe, Arizona 85287-1604, United States

[⊥]Catalan Institution for Research and Advanced Studies (ICREA), Passeig Lluís Companys, 23, 08010, Barcelona, Spain

S *Supporting Information*

ABSTRACT: Incorporation of biotinylated aminopyridine cobalt complexes derived from the triazacyclononane scaffold into the streptavidin protein leads to formation of artificial metalloenzymes for water reduction to hydrogen. The synthesized artificial metalloenzymes have lower overpotential (at the half-peak up to 100 mV) and higher photocatalytic hydrogen evolution activity (up to 14- and 10-fold increase in TOF and TON, respectively, at pH 12.5) than the free biotinylated cobalt complexes. ^{1}H-NMR, EPR and XAS highlight the presence of the metal complexes upon supramolecular attachment to the streptavidin. pH-dependent catalytic studies and molecular dynamics (MD) simulations suggest that the increase in the catalytic activity could be induced by the protein residues positioned close to the metal centers. These findings illustrate the ability of the biotin−streptavidin technology to produce artificial metalloproteins for photo- and electrocatalytic hydrogen evolution reaction.

KEYWORDS: *water reduction to hydrogen, photocatalysis, electrocatalysis, cobalt complexes, streptavidin−biotin*
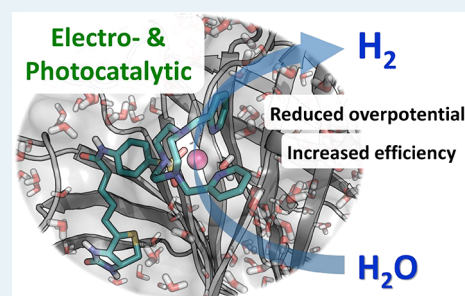
1. INTRODUCTION

Among the possible alternative fuels, molecular hydrogen obtained from light-driven water splitting is ideal from an environmental point of view.[1] However, sustainable generation of hydrogen is extraordinarily challenging and requires a profound understanding of the different reactions involved. In this context, rational design of catalytic systems serves as a tool to interrogate strategies to maximize efficiency and robustness as well as to unravel the mechanistic details.[2] Likewise, nature has served as inspiration by studying and mimicking hydrogenase enzymes, which reversibly catalyze the reduction of protons to molecular hydrogen with high efficiency (turnover frequencies of up to 21 000 s^{-1}).[3]

The high activity of hydrogenases is ascribed in part to the control of the geometry of the active site, the second coordination sphere, and the protection of the catalytic center.[4] However, their characterization and further development for practical applications is a demanding task. Conversely, catalysts active in H$_2$ evolution based on metal complexes are tunable[5] for improving the catalytic activity and overpotentials and increasing the oxygen tolerance. However, most organometallic catalysts are only efficient with strong acids in organic solvents or they are not sufficiently robust in water to be catalytically active. Moreover, control of the second

coordination sphere suffers from significant synthetic challenges, although it is crucial to improve the TOF.[6,7]

In this regard, hybrid natural−artificial systems could serve as testing grounds to study the effect of protein scaffold encapsulation and second-sphere interactions in the catalytic performance of coordination complexes.[3b,8] Several artificial protein−catalysts hybrids have been developed either by assembling synthetic catalysts into the protein pocket[9] or by creating biomimetic systems made by metal substitution and/or mutation.[10] One of the most convenient synthetic approaches builds on supramolecular host−guest interactions, for example, using streptavidin (SA) as a host protein and exploiting its high affinity for biotin (also known as vitamin B7 or vitamin H). SA binds biotin with one of the strongest noncovalent interactions known in nature (dissociation constant (K_d) on the order of ~10^{-14}), ensuring quantitative incorporation of biotinylated molecules.[11] In addition, the biotin−SA complex is resistant to organic solvent, temperature, and pH. On the basis of a concept first reported by Whitesides[12] and further developed by the Ward group, the biotin−SA technology has been applied to create artificial

metalloenzymes for a broad variety of catalytic applications.[13] Very recently, this strategy has also been explored in hydrogen evolution catalysis. It has been observed that the resulting artificial hydrogenases are able to drive H_2 evolution when using $[Ru(bpy)_3]Cl_2$ as a photosensitizer and ascorbate as a sacrificial electron donor, albeit with no significant improvement over the "naked" catalyst.[14]

We recently described a new family of robust, well-defined, and highly tunable aminopyridine cobalt complexes derived from the triazacyclononane (tacn) scaffold for the electro- and photocatalytic H_2 evolution in water.[15] In view of these unique properties and inspired by the previous studies, here we study the encapsulation of two new biotinylated aminopyridine cobalt complexes in SA for photo- and electrocatalytic H_2 production. We found that encapsulation increases the activity significantly under both sets of conditions. Detailed electro- and photochemical pH-dependent hydrogen evolution studies and molecular dynamics (MD) simulations have been performed to elucidate the enhanced catalytic activity observed.

2. RESULTS AND DISCUSSION

We synthesized and studied two new biotinylated cobalt complexes ($\mathbf{Cat^{Bio}}$) based on the 1,4-di(picolyl)-1,4,7-triazacyclononane ($\mathbf{^H Py_2 tacn}$) moiety by employing two different rigid spacer groups for the covalent bond between the biotin and the catalytic center (Figure 1)[15a] in order to investigate the catalytic activity of the cobalt center when positioned inside the protein pocket.[13f,16] The biotin moiety was covalently attached to the tacn backbone either via the secondary nitrogen atom on the tacn ($\mathbf{^{Bio}Py_2 tacn}$) or via a free amine on the spacer group directly linked to the tacn ($\mathbf{^{Bio\text{-}SP}Py_2 tacn}$) through reaction with biotin N-hydroxysuccinimide active ester (NHS-biotin) (Scheme S1).

• **Catalysts (Cat^{Bio})**
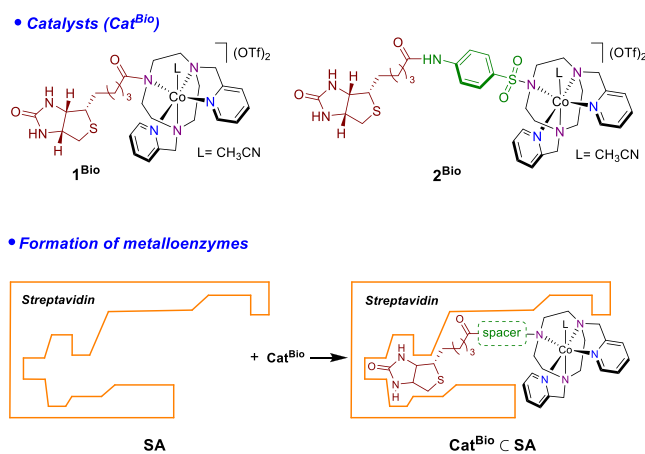

• **Formation of metalloenzymes**

Figure 1. Biotinylated cobalt complexes and artificial metalloenzymes employed in this work.

The biotin-functionalized aminopyridine ligands and complexes $[Co(^{Bio}Py_2 tacn)(MeCN)](OTf)_2$ ($\mathbf{1^{Bio}}$) and $[Co(^{Bio\text{-}SP}Py_2 tacn)(MeCN)](OTf)_2$ ($\mathbf{2^{Bio}}$) (Figure 1) were synthetized adapting a general procedure described in the literature (sections S.1.3 and 1.4).[15a,17] The homologous nonbiotinylated $[Co(^{Amide}Py_2 tacn)(MeCN)](OTf)_2$ ($\mathbf{1^{Amide}}$) and $[Co(^{Amide\text{-}SP}Py_2 tacn)(MeCN)](OTf)_2$ ($\mathbf{2^{Amide}}$) complexes were also synthesized with the aim to study how the absence of biotin affects their behavior (Scheme S1). The synthesis of the ligands $^{Amide}Py_2 tacn$ and $^{Amide\text{-}SP}Py_2 tacn$ was carried out by acylating the free nitrogen atoms of $^H Py_2 tacn$ and $^{NH2\text{-}SP}Py_2 tacn$, respectively (section S.1.3). ^1H NMR spectroscopy, high-resolution electrospray ionization mass spectrometry (HR-MS-ESI), magnetic measurements, and elemental analysis confirm formation of d^7 high-spin ($S = 3/2$) Co^{II} complexes (Figures S1–S7). The cyclic voltammogram (CV) of $\mathbf{1^{Bio}}$ and $\mathbf{1^{Amide}}$ in CH_3CN shows a reversible peak ascribable to the $Co^{II/I}$ couple at -1.09 V (all redox processes are reported vs SCE unless otherwise notified) (Figures S10 and S12). Moreover, the reduction potential for the $Co^{II/I}$ transition in $\mathbf{2^{Bio}}$ (-1.06 V) is close to that of $\mathbf{2^{Amide}}$ (-1.15 V) (Figures S11 and S13). We note that complex $\mathbf{2^{Bio}}$ exhibits an additional irreversible wave at -0.71 V, which can be attributed to reduction of the biotin moiety since it is also observed in the CV of the free $^{Bio\text{-}SP}Py_2 tacn$ ligand and in the biotin (Figures S14–S17).

Incorporation of $\mathbf{1^{Bio}}$ and $\mathbf{2^{Bio}}$ into SA is quantitative, as indicated by the HABA (2-(4′-hydroxyazobenzene)benzoic acid) displacement assay.[16] The linear profile of the HABA displacement by the biotinylated complexes indicates that their affinity for SA is similar to previously reported systems and in the range of that obtained with D-biotin (i.e., $>10^{10}$ M^{-1}, section S.1.5).[16] The stoichiometry of the complex incorporated in the synthesized and isolated metalloenzymes $\mathbf{1^{Bio}}$ $\subset$ SA and $\mathbf{2^{Bio}}$ $\subset$ SA was evaluated by measuring the Co concentration by ICP-MS and the protein concentration by UV–vis. These results are in concordance with previous reports, indicating saturation of the binding sites of the SA employed (SA is a tetramer containing a binding site per unit of monomer). Moreover, the paramagnetic ^1H NMR studies performed with free SA, $\mathbf{2^{Bio}}$, and $\mathbf{2^{Bio}}$ $\subset$ SA indicate that the main proton resonance features of the cobalt complex are present with slight modifications after encapsulation into the SA and that some of the ^1H NMR features of the SA protein are also altered in the $\mathbf{2^{Bio}}$ $\subset$ SA sample, consistent with the supramolecular assembly (Figures S22–S25).

We also studied cobalt K-edge X-ray absorption spectroscopy (XAS) and EPR to provide information about the electronic and geometric structure of the metal coordination environment. The Co K-edge XAS spectra of $\mathbf{2^{Bio}}$ and $\mathbf{2^{Bio}}$ $\subset$ SA have a comparable profile, suggesting a similar coordination environment and oxidation state. The rising edges centered around 7719.3 eV are consistent with a Co^{II} center (Figure S26).[18] Furthermore, the intensity of the pre-edges at 7710.4 eV, of 0.06 normalized units, suggests a centrosymmetric pseudo-octahedral environment.[18a] This is further supported by EPR experiments of $\mathbf{2^{Bio}}$ and $\mathbf{2^{Bio}}$ $\subset$ SA, which at liquid nitrogen temperatures show low-spin Co^{II} signals with g_x and g_y values centered around a g of 2.2 and g_z values approaching 2.0, similar to previously reported values for elongated distorted pseudo-octahedral Co^{II} complexes (Figure S27.B).[6,19] On the other hand, the EPR spectra of $\mathbf{1^{Bio}}$ and $\mathbf{1^{Bio}}$ $\subset$ SA suggest an axially compressed pseudo-octahedral environment at the Co^{II} center with g_z values centered around a g of 2.3 and g_x and g_y values close to 2.0 (Figure S27.A).[6,19] At 15 K the EPR spectra are more informative. The basic EPR features observed in the $[Co(OTf)(^{Ts}Py_2 tacn)](OTf)$ ($\mathbf{2}$), $[Co(Cl)(^{Ts}Py_2 tacn)](Cl)$ $\mathbf{2Cl}$, $\mathbf{1^{Bio}}$ and $\mathbf{2^{Bio}}$ series guide one to understand the EPR of $\mathbf{1^{Bio}}$ $\subset$ SA and $\mathbf{2^{Bio}}$ $\subset$ SA (Table S2). Interestingly, while the EPR spectrum of $\mathbf{2^{Bio}}$ $\subset$ SA is similar to that of $\mathbf{2^{Bio}}$, in the case of $\mathbf{1^{Bio}}$ $\subset$ SA it is essentially different than $\mathbf{1^{Bio}}$. The EPR spectrum of $\mathbf{2^{Bio}}$ $\subset$ SA recorded at 15 K presents three

different Co center environments as for 2^{Bio} (Figure S33). The predominant one corresponds to a Co^{II} high-spin center ($S = 3/2$), and two minor signals can be assigned to low-spin Co^{II} centers coordinated to a different sixth ligand (CH$_3$CN and H$_2$O). In contrast, the main feature in the EPR spectrum of $1^{Bio} \subset SA$ correspond to the rhombic signal with g values centered at 2.37, 2.07, and 2.03, which is in agreement with coordination of a water molecule. This correlates with the fact that the cobalt complex in $1^{Bio} \subset SA$ is more internalized into the protein cavity as judged by the molecular dynamics (MD) simulations (dicussed below). Therefore, the presence of mainly a low-spin Co^{II} rhombic signal may suggest that the protein pocket environment may regulate the binding ligand at the metal center. In the case of the $2^{Bio} \subset SA$, MD simulations show that the cobalt complex is exposed to the protein surface, but it is much more exposed to the reaction media than $1^{Bio} \subset SA$. For both series of complexes the XAS and EPR spectroscopic data indicate only minor electronic and geometric environment modification of the Cat^{Bio} after inclusion into the SA protein. Lastly, incorporation of the cobalt catalyst proceeds, conserving the SA secondary structure, as assessed by CD spectroscopy (Figure S21).

We compared the catalytic activity of these artificial metalloenzymes with the naked biotinylated cobalt complexes 1^{Bio} and 2^{Bio} in the electrochemical reduction of water to H$_2$. The electrochemical measurements were performed at pH ranging from 3.5 to 6 (citrate/NaCl buffer, 100 mM). At pH 3.5 the CV of 1^{Bio} showed a high current intensity irreversible peak with an onset potential at −1.21 V and a maximum at −1.36 V (overpotential (η) = 0.78 V)[20] (Figure 2A, black trace), indicative of a catalytic process. Under the same conditions, complex 2^{Bio} showed similar electrochemical features but shifted to a more negative potential (onset potential about −1.23 V and a maximum at −1.47 V, η = 0.79 V, Figure 2C). The electrocatalytic wave in both complexes (1^{Bio} and 2^{Bio}) displays a pH dependence. The currents appear to follow a nonstandard behavior in the case of 2^{Bio} with a change in slope as the potential is increased. The electrocatalytic peak current (i_c) increases with the proton concentration (Figures S35 and S36), suggesting that the rate-determining step of the catalytic process relies on a proton transfer from water.[21] The onset, the peak potential for proton reduction (E_p), and the half peak ($E_{1/2}$) of 1^{Bio} shift toward less negative potentials when increasing the proton concentration, following a PCET (proton-coupled electron transfer) reaction (Figure 2 and Figure S46).[22] The Nernstian response was found to be −37 mV per pH unit (Figure 2B), close to expected for a 2-electron and 1-proton reduction process (−30 mV per pH). This value is qualitatively similar to the −26 mV per pH unit reported for a Co(Py5) system[21b] or to the −24 mV per pH unit observed in cobalt diamine systems.[21a] Complex 2^{Bio} reveals only a minor dependence of the E_p and onset potential with the pH (Figure 2D). The molecular behavior of 1^{Bio} and 2^{Bio} was confirmed by rinsing tests (Figure S36), which indicates the absence of active species attached to the electrode surface.[23] Furthermore, the catalytic current shows a first-order dependence on the catalyst concentration[24] (Figure S37) similarly to what was observed for the parent complex 2.[15a]

The electrochemical properties of $Cat^{Bio} \subset SA$ were interrogated as a thin film,[3a,9c,10a,25] prepared by drop casting over a glassy carbon electrode and carbon cloth (see sections S.1.7 and S.1.8), which yields an intense electrocatalytic wave
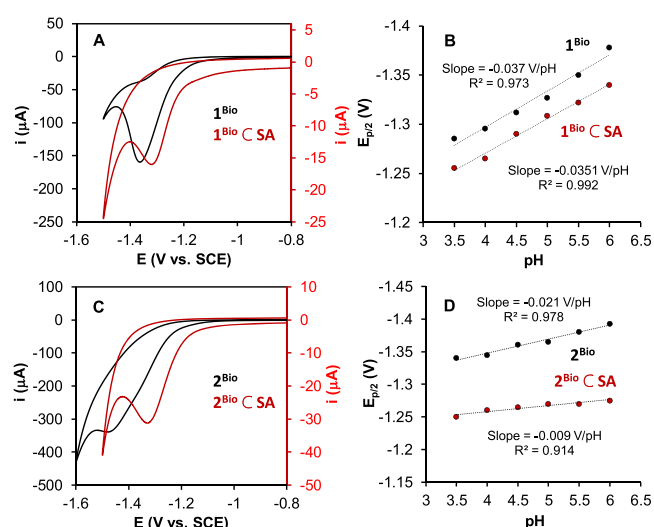

Figure 2. CV of (A) 1^{Bio} (1 mM, black trace) and $1^{Bio} \subset SA$ (thin film, red trace) and (C) 2^{Bio} (1 mM, black trace) and $2^{Bio} \subset SA$ (thin film, red trace) (see section S.1.7 for detailed experimental conditions). Plot of the half intensity of the catalytic peak potential (E_p) as a function of pH of (B) 1^{Bio} (1 mM) and $1^{Bio} \subset SA$ (thin film) and (D) 2^{Bio} (1 mM) and $2^{Bio} \subset SA$ (thin film).

(Figure S38). For comparison, we also analyzed and compared the CV of $2^{Bio} \subset SA$ (73 μM) in solution, which gives similar results under the same experimental conditions (Figure S39). When the cathodic scan was performed in the presence of naked SA the observed current was negligible at this redox potential (Figure S38), indicating that the catalytic wave observed for $Cat^{Bio} \subset SA$ is due to the hosted Cat^{Bio}. The reduction potential of the reduction peak did not change with the amount of protein deposited on a carbon cloth electrode, suggesting that protein−protein interactions possible in the film do not interfere in the redox process (Figure S40). The catalytic activity of the $Cat^{Bio} \subset SA$ adducts display a pH dependence (Figures S42 and S43) comparable to that obtained with the Cat^{Bio} and Cat^{Amide} catalysts (Figures S35, S36, S44−S48, S55, and S56). A clear shift in the redox potential of the catalytic value (ΔE_p, $\Delta E_{p/2}$, and onset potential) was observed when the Cat^{Bio} were incorporated into the host SA. The magnitude of the redox potential shift when the current intensity is one-half of the value regarding the current intensity at the maximum of the catalytic peak ($\Delta E_{p/2}$) varies with the pH value and ranges between 20 and 30 mV for 1^{Bio} and $1^{Bio} \subset SA$ (Figure 2B) and between 60 and 100 mV for 2^{Bio} and $2^{Bio} \subset SA$ (Figure 2D) (Figures S44−S46). This result is in sharp contrast with those previously reported for some artificial metalloenzymes based on cobalt complexes.[9c,10a,e] For instance, incorporating cobaloxime derivatives into the heme pocket of apo sperm-whale myoglobin results in a negative shift of about 100 mV, increasing the overpotential.[9c] Conversely, the positive direction of the shift observed for our systems suggests beneficial interactions of the SA pocket with the catalyst (presumably the secondary coordination sphere) that reduces the water reduction overpotential. However, a direct comparison of current density is not straightforward since the protein concentration on the electrode is unknown.

To verify the formation of H$_2$ we performed controlled potential electrolysis (CPE) at −1.4 V during 3 h under static conditions for 2^{Bio} and $2^{Bio} \subset SA$ (Figures S49−S51). In both
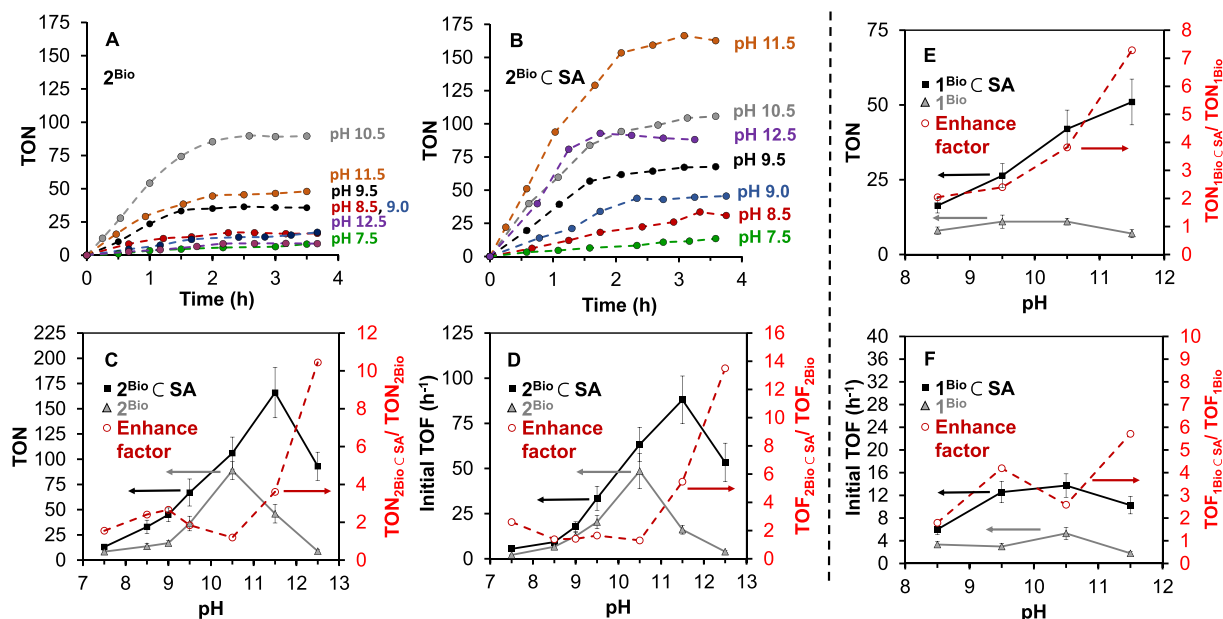
Figure 3. Photoinduced H_2 production at different pH values for reaction of Cat^{Bio} and $Cat^{Bio} \subset SA$ (5 μM in Co), PS_{Ir} (250 μM), TEOA (0.4 M) in 0.4 mL of $CH_3CN:H_2O$ (3:7 v/v) containing phosphate buffer (100 mM) and NaCl (100 mM) after 4 h irradiation (1100 W·m^{-2}, λ > 400 nm). Time traces of H_2 evolved using (A) 2^{Bio} and (B) $2^{Bio} \subset SA$. (C) TON for 2^{Bio} (gray) and $2^{Bio} \subset SA$ (black) and $TON_{2Bio \subset SA}/TON_{2Bio}$ (red). (D) Initial TOF (h^{-1}) for 2^{Bio} (gray), $2^{Bio} \subset SA$ (black), and $TOF_{2Bio \subset SA}/TOF_{2Bio}$ (red). (E) TON for 1^{Bio} (gray) and $1^{Bio} \subset SA$ (black) and $TON_{1Bio \subset SA}/TON_{1Bio}$ (red). (F) Initial TOF (h^{-1}) for 1^{Bio} (gray), $1^{Bio} \subset SA$ (black), and $TOF_{1Bio \subset SA}/TOF_{1Bio}$ (red). Error bars are average of two duplicates.

cases H_2 was detected by sampling the headspace of the electrochemical cell after the CPE and subjecting the sample to chromatographic analysis (gas chromatography-thermal conductivity detector, GC-TCD). In the case of $2^{Bio} \subset SA$, after an initial current decrease it remains about constant for the rest of the experiment with good Faraday yield. In contrast, under the same CPE conditions, 2^{Bio} yields about 560 TON of H_2 with good Faraday yield, but suffers a fast and intense activation process during the CPE, leading to a higher current density (Figure S51). This is indicative of the formation of a more active species. A CV after the CPE with a clean GC electrode did not show any wave in the CV at the Co$^{II/I}$ redox couple 2^{Bio}. In contrast, after 3 h of CPE the CV of the $2^{Bio} \subset SA$ solution presents a wave, although shifted and significantly reduced.

We hypothesized that the observed difference in activity between Cat^{Bio} and $Cat^{Bio} \subset SA$ is due to secondary sphere interactions with the protein scaffold. To rule out other possibilities, such as coordination of biotin to the cobalt center, we also studied the electrochemical behavior of model complexes 1^{Amide} and 2^{Amide}. We found that 1^{Amide} and 2^{Amide} exhibit similar electrochemical behaviors (Co$^{II/I}$ redox couples and pH behavior) to the Cat^{Bio} homologous complexes. In addition, the cyclic voltammograms of 1^{Amide} and 2^{Amide} in CH_3CN shows negligible changes upon addition of large amounts of esterified biotin (up to 20 equiv, biotin was esterified for solubility reasons, Figures S53 and S54). We also studied computationally (B3LYP-3D/6−31+G** level of theory) the possible coordination modes for the N, O, and S atoms of biotin to the cobalt center in oxidation states I and II. All optimized structures showed that intramolecular coordination of biotin to the cobalt center is largely endergonic. In addition, an exchange between a coordinated pyridine (or tacn backbone) and a N, O, or S atom of biotin is also highly endergonic (Figures S79−S81 and S84−S86). The bimolecular

biotin interactions appear negligible as there is a linear correlation between the current intensity and the Cat^{Bio} concentration (vide supra). All of these observations together with the XAS, EPR and catalysis show no coordination of biotin to the cobalt center and indicate that the ΔE_p observed between Cat^{Bio} and $Cat^{Bio} \subset SA$ arises form second coordination sphere interactions between the catalytic center and the protein pocket.

We also investigated whether the catalytic activity of 1^{Bio} and 2^{Bio} could be influenced by protein encapsulation in light-driven H_2 evolution. The catalytic activity of 2^{Bio} and $2^{Bio} \subset SA$ was studied by irradiation (1100 W·m^{-2} of visible light, λ > 400 nm) of a solution containing the catalysts (5 μM), [Ir(ppy)$_2$(bpy)]PF$_6$ (PS_{Ir}) (250 μM) and TEOA (0.4 M).[26,15a] Due to the low solubility of PS_{Ir} in water, 30% in volume of MeCN was used as a cosolvent. We verified the stability of $2^{Bio} \subset SA$ by monitoring its secondary structure by CD at increasing concentrations of CH_3CN. No changes in the CD were observed up to 50% of cosolvent (Figures S57 and S58) nor in all of the pH range studied (Figures S59−S62).

Hydrogen evolution was monitored as a function of time by analysis of aliquots from the reaction cuvette headspace by gas chromatography at different pH values adjusted with phosphate buffer (100 mM). The pH of the buffer solutions was measured and adjusted (when needed) after addition of TEOA using NaOH or HCl. The catalytic activity of 2^{Bio} raises from pH 7 to a maximum at about pH 10.5 (TON, 89; TOF, 49·h^{-1}; Figure 3).[27] For $2^{Bio} \subset SA$ the catalytic activity was higher than for 2^{Bio} at all pH values, and the maximum in catalytic activity changes from pH 10.5 to 11.5 (Table S4). A pH bell-shaped profile is observed for the catalytic activity of both 2^{Bio} and $2^{Bio} \subset SA$ (Figure 3). This bell shape has been previously observed in photocatalytic systems such as Ru/ascorbate[28] and fluorescein/Et$_3$N.[29] The stablished reason for this catalytic activity pH behavior is that at lower pH the

effective electron donor concentration (TEOA) is reduced, while at higher pH values the catalytic activity decreases due to the lower concentration of protons available, resulting in the catalytic activity vs pH in a bell-shaped profile.

The difference in the catalytic activity between 2^{Bio} and 2^{Bio} C SA increases at higher pH values. At pH 12.5 the catalytic activity of 2^{Bio} C SA is 10- and 14-fold higher in terms of TON and TOF, respectively, than the values obtained for 2^{Bio}. Moreover, at pH 12.5 the catalytic activity of 2^{Bio} is negligible. This behavior may be rationalized if it is considered that the protein protects the cobalt center and alters the effective available protons for the metal protonation regarding the pH. Nevertheless, this is a very complex system, and other possible contributions to the observed behavior cannot be discarded. It is important to note that protonation of the Co^I species to give $Co^{III}-H$ is thought to be the rate-limiting step in cobalt-based catalysts at basic pH values.[15a]

Although 1^{Bio} shows lower catalytic activity than 2^{Bio}, the catalytic enhancement by the protein environment is also remarkable with an enhancement factor in TON at pH 11.5 of 7.3 (1^{Bio} C SA) and 3.6 (2^{Bio} C SA), suggesting a better protecting effect by the protein pocket due to the absence of the spacer (Figure 3E and 3F and Table 1). Moreover, control

Table 1. Photocatalytic Activities of 2^{Bio} and 2^{Bio} C SA at pH 11.5[a]

	1^{Bio}	1^{Bio} C SA	2^{Bio}	2^{Bio} C SA
TON	7	51	46	166
$TON_{CatBio C SA}/TON_{CatBio}$	7.3		3.6	
TOF	1.8	10.3	16	88
$TOF_{CatBio C SA}/TOF_{CatBio}$	5.7		5.5	

[a]Cobalt catalyst (5 μM in Co) PS_{Ir} (250 μM), TEOA (0.4 M) in 0.4 mL of $CH_3CN:H_2O$ (3:7 v/v) containing phosphate buffer (100 mM) and NaCl (100 mM) (pH 11.5) after 4 h irradiation (1100 W·m^{-2}, λ > 400 nm).

experiments performed generating the metalloenzyme in situ before catalysis (by mixing 2^{Bio} with SA ~30 min before the catalysis) show the same catalytic activity as the presynthesized and purified 2^{Bio} C SA (Figure S65). In contrast, addition of SA to complex 2^{Amide} does not affect its photocatalytic activity (Figure S66), pointing toward an enhancement in the H_2 production activity due to supramolecular interactions in 2^{Bio} C SA.

We also performed photochemical studies using [Cu-(xantphos)(bathocuproine)]PF$_6$ (PS_{Cu}) as photoredox catalyst and triethylamine (Et$_3$N) as electron donor in nonbuffered solutions (Figure 4). Under these catalytic conditions we found that the H_2 evolution catalytic performance for the metalloproteins (Cat^{Bio} C SA) is higher than for the Cat^{Bio} in terms of both TOF and TON. Also, a remarkably higher quantity of hydrogen is formed than in the case of using the Ir photosensitizer (PS_{Ir}) in combination with TEOA.

We performed molecular dynamics (MD) simulations of streptavidin in complex with 1^{Bio} and 2^{Bio} to evaluate their binding modes and identify which residues play a crucial role on catalytic enhancement (see SI for computational details). These calculations do not capture protein−protein interactions and therefore are only relevant for isolated proteins such as the conditions employed in this study. Representative conformations sampled along the accumulated 750 ns of MD simulations (i.e., three replicas of 250 ns for each case) reveal
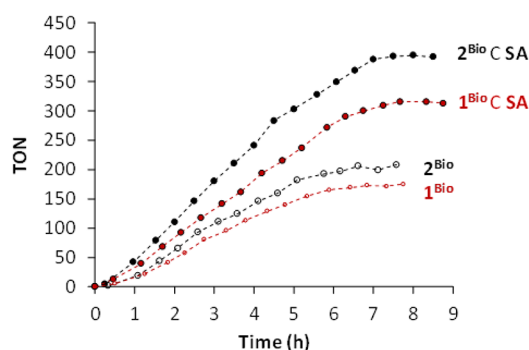

Figure 4. Traces of the photoinduced H_2 production by (from top to bottom) 2^{Bio} C SA, 1^{Bio} C SA, 2^{Bio}, and 1^{Bio} (5 μM) together with PS_{Cu} (250 μM), Et$_3$N (0.15 M) in 0.4 mL of $CH_3CN:H_2O$ (3:7 v/v) after 9 h irradiation (1100 W·m^{-2}, λ > 400 nm).

a high affinity of the protein toward 1^{Bio} and 2^{Bio}. The presence of a spacer group between the biotin and the catalytic center in 2^{Bio} confers additional flexibility to the ligand, leading to two main different conformations (Figure S70). As in biotin−SA complex, tryptophan residues (Trp79, Trp92, Trp108) bind the ligand through CH··· π interactions (the mean distance between the center of mass of Trp108 and biotin rings is ca. 4.0 Å for both 1^{Bio} and 2^{Bio}, see Figure 5).[30]

To gain insights into the origin of the improvement in catalytic activity, we evaluated the conformational dynamics of the binding pocket in the presence of 1^{Bio} and 2^{Bio} (Figure 5). Polar residues around the cobalt complex together with the assistance of water could promote the catalysis. Both 1^{Bio} and 2^{Bio} are exposed to several solvent molecules (ca. 3−5 waters in 1^{Bio} and 2−4 waters in 2^{Bio}, Figures S69 and S72). In addition, many polar residues that could act as a proton donor or activate a water molecule to promote metal protonation are found close to the ligand (Figure 5). 1^{Bio} shows low flexibility during the MD simulations, sampling most of the time the same conformation, which positions the cobalt center near polar Ser112, Ser88, Glu51, and Asn49 residues (S67 and S68). In contrast, 2^{Bio} is more flexible and adopts two different conformations during the MD simulations (the bend conformation highlighted in the square of Figure 5 and extended conformation of Mon3 in S34A). In the bend conformation, the metal center is situated close to polar residues Ser112 and Leu124 (Figure 5). For most of the simulation time the hydrophobic residue Leu124 in the bend conformation is near the metal center (Figures 5 and S71), suggesting that this residue could be mutated to enhance activity. In contrast, in the extended conformation, the metal center is close to the polar residues Asn49 and His87 (Figures S70E and S71). We investigated whether the flexibility of the metal complexes is restricted upon encapsulation by performing MD simulations for 1^{Bio} and 2^{Bio} in solution. In the absence of protein, both complexes have a certain flexibility. However, complex 2^{Bio}, with the longer link, is the most flexible one, as indicated by the computed root-mean square deviations (RMSD, see Figure S74). The higher flexibility of 2^{Bio} is also retained upon protein encapsulation (compare RMSD of 1^{Bio} and 2^{Bio} inside the protein, Figures S75 and S76), which allows a higher water accessibility, consistent with the water shell and $g(r)$ analysis (Figure S73).
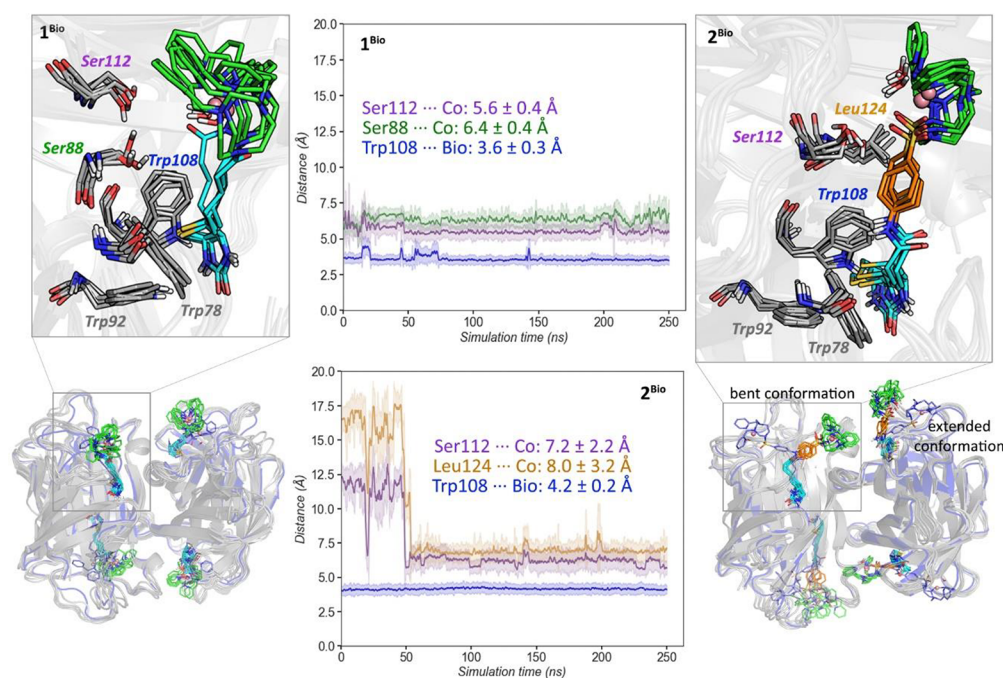
Figure 5. Overlay of representative snapshots visited along the MD simulations for 1^{Bio} and 2^{Bio}. Conformational dynamics of the binding pockets are also shown, where the most important residues surrounding the biotin complexes are represented together with some selected distances (in Angstroms). Distances have been computed from the metal center and either the side chain of Ser112, Ser88 (oxygen atom, in purple and green, respectively), and Leu25 (terminal carbon of isobutyl side chain, orange). Trp108−biotin distance is computed between the center of mass of the indole ring of Trp108 and the tetrahydrothiophene ring of biotin (in blue). Mean distances and standard deviations are also included (in Angstroms).

3. CONCLUSIONS

In conclusion, we prepared new cobalt artificial metalloenzymes based on the biotin−streptavidin technology and able to reduce water to hydrogen under electro- and photochemical conditions. We found that incorporation of the cobalt catalysts into the streptavidin scaffold results in several beneficial effects, especially in the 2^{Bio} catalyst. It reduces the overpotential for electrocatalytic hydrogen production and increases the light-driven hydrogen production rate and turnover numbers. This work demonstrates a straightforward and successful strategy to enhance the catalytic activity for water reduction to H_2. Future studies will be performed to extend such cobalt artificial metalloenzymes to various other photocatalytic chemical transformations.

4. EXPERIMENTAL SECTION

Materials and Reagents. Reagents and solvents were purchased from commercial sources and used as received unless otherwise stated. Triethylamine (Et_3N, ≥99% purity) and triethanolamine (TEOA, ≥99% purity) were purchased from Sigma-Aldrich and used without further purification. Photosensitizer $[Ir(bpy)(ppy)_2]PF_6$ (PS_{Ir}) was synthesized according to literature procedures.[26a] Ethyl [(3aS,4S,6aR)-2-oxo-hexahydrothieno[3,4-d]imidazole-4-yl]pentanoate (^{COOEt}Biotin) was synthesized following the reported method from the literature.[31] Anhydrous acetonitrile was purchased from Scharlab. Water (18.2 MΩ·cm) was purified with a Milli-Q Millipore Gradient AIS system. All solvents were thoroughly degassed and stored under anaerobic conditions.

Physical Methods. *UV−vis Spectroscopy.* UV−vis spectra were acquired on a Varian Cary 50 Bio Spectrophotometer.

Gas Chromatography. Gas chromatography was carried out on a SRI instruments, model 310C, GC using a 5 Å molecular sieve column with a thermal conductivity detector and argon carrier gas.

Nuclear Magnetic Resonance. All NMR spectra were recorded in $CDCl_3$ on a Varian 400 or 500 MHz instrument, as noted.

Circular Dichroism. Spectra measurements were carried out on an Applied Photophysics Chirascan Circular Dichroism spectrometer equipped with a photomultiplier detector, dual-polarizing prism design monochromator, photoelastic modulator (PEM), and 150 W xenon light source. An average of 3 scans per sample were measured.

X-ray Diffraction. Crystals of 1^{Amide} were grown by slow diffusion of Et_2O to a CH_2Cl_2 solution of the complex. The crystals for these samples were selected using a Zeiss stereomicroscope using polarized light and prepared under inert conditions immersed in perfluoropolyether as protecting oil for manipulation. Crystal structure determinations for 1^{Amide} were carried out using a Apex DUO Kappa 4-axis goniometer equipped with an APPEX 2 4K CCD area detector, a Microfocus Source E025 IuS using Mo Kα radiation, Quazar MX multilayer optics as monochromator, and an Oxford Cryosystems low-temperature device Cryo-stream 700 plus ($T = -173$ °C). On the Bruker device, the following programs were used: Data collection APEX-2,[32] data reduction Bruker Saint[33] V/.60A, and absorption correction SADABS[34] or TWINABS.[35] The crystal structure solution was achieved using the computer program SHELXT.[36] Visualization was performed with the program SHELXle.[37] Missing atoms were subsequently located from difference Fourier synthesis and added to the atom list. Least-squares refinement on F^2 using all measured intensities was carried out using the

program SHELXL 2015.[38] All non-hydrogen atoms were refined including anisotropic displacement parameters.

Cyclic Voltammetry. Electrochemical experiments were carried out on a CH instruments 1242B potentiostat and with a VSP potentiostat from Bio-Logic, equipped with the EC-Lab software. The experiments were performed under inert (Ar) atmosphere in a custom double-wall jacketed single-compartment cell. For all electrochemical measurements, a three-electrode system was used: a 3 mm diameter glassy carbon working electrode with a surface area of 0.28 cm², a platinum mesh counter electrode, and a saturated calomel reference electrode, unless otherwise specified. Working electrodes were polished with 1 μM alumina for 5 min, followed by 10 min of sonication, prior to use. Cyclic voltammetry was carried out on samples prepared in 100 mM citrate and 25 mM NaCl buffer of desired pH (3.5, 4.0, 4.5, 5.0, 5.5, and 6.0); scans were performed at a 100 mV·s⁻¹ scan rate. All potentials are quoted versus SCE. All electrolyte solutions were degassed by freeze and pump techniques. Samples were prepared by diluting the catalyst from a stock solution (10 mM) in water containing 5% DMSO to solubilize the catalyst. The final percentage of DMSO in the electrochemical cell was 0.5%. Electrochemical experiments **Cat^Bio C** SA were done by preparing a thin film of **Cat^Bio C** SA over the glassy carbon electrodes (0.28 cm² surface area) by drop casting of 10 μL of a stock solution of metalloprotein of 10 μM and drying, otherwise indicated. After drying, electrochemical measurements were performed by directly submerging the glassy carbon electrode into the solution.

Electron Paramagnetic Resonance. An EMX Micro X-band EPR spectrometer from Bruker was used to collect data on 0.35 mM solution samples in a mixture of aqueous buffer and MeCN (7:3, buffer = Tris·HCl 100 mM, pH 7.5) using a finger Dewar at 77 K and He cryostat from Oxford Instruments at 50 and 15 K. Data was acquired in perpendicular mode with a modulation frequency of 100 KHz, a modulation amplitude of 10 G, a 10.24 ms time constant, and 19.02 ms conversion time with a microwave power was 0.1851 mW. Spectra were simulated using the EasySpin software package.[39]

X-ray Absorption Spectroscopy. All NM Samples were recorded as 0.35 mM solutions in a mixture of aqueous buffer and MeCN (7:3, buffer = Tris·HCl 100 mM, pH 7.5) at the SOLEIL synchrotron (2.75 GeV, 400mA storage ring) SAMBA Beamline equipped with a helium cryostat (20 K) and using a Si(220) double-crystal monochromator together with a 36 channel Ge detector. Data calibration and normalization was carried out using the Athena software package.[40] Energies were calibrated to the first inflection point of Co foil spectra set at 7709.5 eV. A linear pre-edge function and a quadratic polynomial for the postedge were used for background subtraction and normalization of the edge jump.

Photoinduced H₂ Evolution. Photoinduced H₂ production irradiation was performed using a 450W xenon lamp with a 400 nm cutoff filter, irradiating at a constant 1100 W/m² throughout the experiment. For each experiment, 400 μL of a reaction mixture containing all of the reagents was added to an airtight 1 mm cuvette and degassed extensively with argon prior to illumination. During irradiation time course 100 μL samples of the headspace were removed with a gastight syringe and injected directly for analysis by GC. A GC calibration curve was obtained by injecting various volumes of a 1% H₂, 99% N₂ gas mixture. The pH of the buffer solutions was measured and adjusted (if needed) after addition of TEOA by addition NaOH or HCl.

Theoretical Calculations. *DFT Calculations.* We studied the coordination ability of the biotinated ligands ^Bio**Py₂tacn** and ^Bio-SP**Py₂tacn** to the metal center and the possibility of binding the biotin fragment to the metal center in complexes **1^Bio** and **2^Bio** computationally by density functional theory (DFT) using the Gaussian09 program.[41] Geometry optimizations were performed in the unrestricted spin formalism, with the B3LYP hybrid exchange-correlation functional[42] and the standard 6-31+G** 6d basis set for all atoms. An extra quadratic convergent SCF step was added when the first-order SCF did not converge ("scf = xqc" keyword). The solvation effect of acetonitrile was introduced in geometry optimizations and energy through the IEFPCM-SMD polarizable continuum model.[43] Dispersion effects were also included using the Grimme D₃ correction.[44] The geometries have been edited with the Chemcraft program.[45] The located stationary points were characterized by analytical frequency calculations at the same level of theory as geometry optimizations. Gibbs energy values (G) were obtained by including thermal, solvation, and Grimme corrections to the potential energy computed with the 6-31+G** 6d basis set on equilibrium geometries.

Molecular Dynamics Simulations. MD simulations in explicit water were performed using the AMBER 16 package[46] on our in-house GPU cluster Galatea. **1^Bio** and **2^Bio** parameters for the MD simulations were generated within the *antechamber* module of AMBER 16 using the general AMBER force field (GAFF).[47] We used the bonded model for the Co (quadruplet state as the lowest in energy) and ligand moiety; in particular, we used the Seminario method approach to obtain the metal parameters needed for the simulation as implemented in Prof. Ryde's program.[48] The optimization, frequencies, and partial charge were set to fit the electrostatic potential generated at the UB3LYP/6-31G(d) level by the restrained electrostatic potential (RESP) model using Gaussian 09. The charges were calculated according to the Merz−Singh−Kollman scheme. We docked **1^Bio** and **2^Bio** complexes in the biotin pocket using the pair-fitting tool in Pymol (http://www.pymol.org) using the biotin moiety of the crystal structure (PDB 1MK5) as a reference and the optimized structure of the complex creating the tetramer enzyme. Amino acid protonation states and the data needed for the electrostatic map were set up using the Propka3.0 server (http://nbcr-222.ucsd.edu/pdb2pqr_2.0.0/).[49] Then the enzyme was solvated in a pre-equilibrated truncated cuboid box with a 10 Å buffer of TIP3P[50] water molecules using the AMBER16 leap module, resulting in the addition of ca. 9000 solvent molecules. The systems were neutralized by addition of explicit counterions (Na⁺ and Cl⁻). All subsequent calculations were carried out using the widely tested Stony Brook modification of the Amber 99 force field (ff14SB).[51] The structure used was 1MK5 from the protein data bank (PDB).

A two-stage geometry optimization was performed. The first stage minimizes the positions of solvent molecules and ions imposing positional restraints on solute by a harmonic potential with a force constant of 500 kcal mol⁻¹ Å⁻², and the second stage is an unrestrained minimization of all of the atoms in the simulation cell. The systems are gently heated using six 50 ps steps, incrementing the temperature 50 K each step (0−300 K) under constant volume and periodic boundary conditions. Water molecules were treated with the SHAKE algorithm such that the angle between the hydrogen atoms is

kept fixed. Long-range electrostatic effects were modeled using the particle-mesh-Ewald method.[52]

A 8 Å cutoff was applied to Lennard—Jones and electrostatic interactions. Harmonic restraints of 10 kcal·mol^{-1} were applied to the solute, and the Langevin equilibration scheme was used to control and equalize the temperature. The time step was kept at 1 fs during the heating stages, allowing potential inhomogeneities to self-adjust. Each system was then equilibrated without restrains for 2 ns with a 2 fs time step at a constant pressure of 1 atm and temperature of 300 K. After the systems were equilibrated in the NPT ensemble, 3 independent 250 ns MD simulations for 1^{Bio} and 2^{Bio} (i.e., 750 μs accumulated) were performed under the NVT ensemble and periodic-boundary conditions.

ASSOCIATED CONTENT

Ⓢ Supporting Information

The Supporting Information is available free of charge on the ACS Publications website at DOI: 10.1021/acscatal.8b04981.

> Synthesis and characterization of ligands, catalysts, and SA adducts; determination of electro- and photocatalytic performance; DFT and molecular dynamic simulations (PDF)

AUTHOR INFORMATION

Corresponding Authors
*E-mail: gghirlanda@asu.edu
*E-mail: jlloret@iciq.es

ORCID Ⓘ
Arnau Call: 0000-0003-0970-7195
Sílvia Osuna: 0000-0003-3657-6469
Julio Lloret-Fillol: 0000-0002-4240-9512

Author Contributions
‡A.C. and C.C.: These authors ontributed equally.

Notes
The authors declare no competing financial interest.

REFERENCES

(1) (a) Barber, J.; Tran, P. D. From Natural to Artificial Photosynthesis. *J. R. Soc., Interface* **2013**, *10*, 20120984. (b) Lewis, N. S.; Nocera, D. G. Powering the Planet: Chemical Challenges in Solar Energy Utilization. *Proc. Natl. Acad. Sci. U. S. A.* **2006**, *103*, 15729−15735.

(2) (a) McKone, J. R.; Marinescu, S. C.; Brunschwig, B. S.; Winkler, J. R.; Gray, H. B. Earth-abundant Hydrogen Evolution Electrocatalysts. *Chem. Sci.* **2014**, *5*, 865−878. (b) Du, P.; Eisenberg, R. Catalysts Made of Earth-abundant Elements (Co, Ni, Fe) for Water Splitting: Recent Progress and Future Challenges. *Energy Environ. Sci.* **2012**, *5*, 6012−6021. (c) Artero, V.; Chavarot-Kerlidou, M.; Fontecave, M. Splitting Water with Cobalt. *Angew. Chem., Int. Ed.* **2011**, *50*, 7238−7266. (d) Le Goff, A.; Artero, V.; Jousselme, B.; Tran, P. D.; Guillet, N.; Metaye, R.; Fihri, A.; Palacin, S.; Fontecave, M. From Hydrogenases to Noble Metal-free Catalytic Nanomaterials for H$_2$ Production and Uptake. *Science* **2009**, *326*, 1384−1387.

(3) (a) Lubitz, W.; Ogata, H.; Rudiger, O.; Reijerse, E. Hydrogenases. *Chem. Rev.* **2014**, *114*, 4081−4148. (b) Simmons, T. R.; Berggren, G.; Bacchi, M.; Fontecave, M.; Artero, V. Mimicking Hydrogenases: From Biomimetics to Artificial Enzymes. *Coord. Chem. Rev.* **2014**, *270−271*, 127−150. (c) Tard, C.; Pickett, C. J. Structural and Functional Analogues of the Active Sites of the [Fe]-, [NiFe]-, and [FeFe]-Hydrogenases. *Chem. Rev.* **2009**, *109*, 2245−2274.

(4) (a) Mulder, D. W.; Shepard, E. M.; Meuser, J. E.; Joshi, N.; King, P. W.; Posewitz, M. C.; Broderick, J. B.; Peters, J. W. Insights into [FeFe]-hydrogenase Structure, Mechanism, and Maturation. *Structure* **2011**, *19*, 1038−1052. (b) Knörzer, P.; Silakov, A.; Foster, C. E.; Armstrong, F. A.; Lubitz, W.; Happe, T. Importance of the Protein Framework for Catalytic Activity of [FeFe]-hydrogenases. *J. Biol. Chem.* **2012**, *287*, 1489−1499. (c) Berggren, G.; Adamska, A.; Lambertz, C.; Simmons, T. R.; Esselborn, J.; Atta, M.; Gambarelli, S.; Mouesca, J. M.; Reijerse, E.; Lubitz, W.; Happe, T.; Artero, V.; Fontecave, M. Aiomimetic Assembly and Activation of [FeFe]-hydrogenases. *Nature* **2013**, *499*, 66−69. (d) Esselborn, J.; Lambertz, C.; Adamska-Venkatesh, A.; Simmons, T.; Berggren, G.; Noth, J.; Siebel, J.; Hemschemeier, A.; Artero, V.; Reijerse, E.; Fontecave, M.; Lubitz, W.; Happe, T. Spontaneous Activation of [FeFe]-hydrogenases by an Inorganic [2Fe] Active Site Mimic. *Nat. Chem. Biol.* **2013**, *9*, 607−609.

(5) (a) Zee, D. Z.; Chantarojsiri, T.; Long, J. R.; Chang, C. J. Metal-polypyridyl Catalysts for Electro- and Photochemical Reduction of Water to Hydrogen. *Acc. Chem. Res.* **2015**, *48*, 2027−2036. (b) Queyriaux, N.; Jane, R. T.; Massin, J.; Artero, V.; Chavarot-Kerlidou, M. Recent Developments in Hydrogen Evolving Molecular Cobalt(II)-polypyridyl Catalysts. *Coord. Chem. Rev.* **2015**, *304−305*, 3−19.

(6) (a) Jian, J. X.; Liu, Q.; Li, Z. J.; Wang, F.; Li, X. B.; Li, C. B.; Liu, B.; Meng, Q. Y.; Chen, B.; Feng, K.; Tung, C. H.; Wu, L. Z. Chitosan Confinement Enhances Hydrogen Photogeneration from a Mimic of the Diiron Subsite of [FeFe]-hydrogenase. *Nat. Commun.* **2013**, *4*, 1−9. (b) Singleton, M. L.; Reibenspies, J. H.; Darensbourg, M. Y. A Cyclodextrin Host/Guest Approach to a Hydrogenase Active Site Biomimetic Cavity. *J. Am. Chem. Soc.* **2010**, *132*, 8870−8871.

(7) (a) Orain, C.; Quentel, F.; Gloaguen, F. Photocatalytic Hydrogen Production Using Models of the Iron-iron Hydrogenase Active Site Dispersed in Micellar Solution. *ChemSusChem* **2014**, *7*, 638−643. (b) Pullen, S.; Fei, H.; Orthaber, A.; Cohen, S. M.; Ott, S. Enhanced Photochemical Hydrogen Production by a Molecular Diiron Catalyst Incorporated into a Metal-organic Framework. *J. Am. Chem. Soc.* **2013**, *135*, 16997−17003. (c) Yu, T.; Zeng, Y.; Chen, J.; Li, Y. Y.; Yang, G.; Li, Y. Exceptional Dendrimer-based Mimics of Diiron Hydrogenase for the Photochemical Production of Hydrogen. *Angew. Chem., Int. Ed.* **2013**, *52*, 5631−5635.

(8) (a) Faiella, M.; Roy, A.; Sommer, D.; Ghirlanda, G. De NovoDesign of Functional Proteins: Toward Artificial Hydrogenases.

Biopolymers **2013**, *100*, 558−571. (b) Bos, J.; Browne, W. R.; Driessen, A. J. M.; Roelfes, G. Supramolecular Assembly of Artificial Metalloenzymes Based on the Dimeric Protein LmrR as Promiscuous Scaffold. *J. Am. Chem. Soc.* **2015**, *137*, 9796−9799.

(9) (a) Soltau, S. R.; Niklas, J.; Dahlberg, P. D.; Poluektov, O. G.; Tiede, D. M.; Mulfort, K. L.; Utschig, L. M. Aqueous Light Driven Hydrogen Production by a Ru−ferredoxin−Co Biohybrid. *Chem. Commun.* **2015**, *51*, 10628−10631. (b) Onoda, A.; Kihara, Y.; Fukumoto, K.; Sano, Y.; Hayashi, T. Photoinduced Hydrogen Evolution Catalyzed by a Synthetic Diiron Dithiolate Complex Embedded within a Protein Matrix. *ACS Catal.* **2014**, *4*, 2645−2648. (c) Bacchi, M.; Berggren, G.; Niklas, J.; Veinberg, E.; Mara, M. W.; Shelby, M. L.; Poluektov, O. G.; Chen, L. X.; Tiede, D. M.; Cavazza, C.; Field, M. J.; Fontecave, M.; Artero, V. Cobaloxime-based Artificial Hydrogenases. *Inorg. Chem.* **2014**, *53*, 8071−8082. (d) Silver, S. C.; Niklas, J.; Du, P.; Poluektov, O. G.; Tiede, D. M.; Utschig, L. M. Protein Delivery of a Ni Catalyst to Photosystem I for Light-driven Hydrogen Production. *J. Am. Chem. Soc.* **2013**, *135*, 13246−13249. (e) Berggren, G.; Adamska, A.; Lambertz, C.; Simmons, T. R.; Esselborn, J.; Atta, M.; Gambarelli, S.; Mouesca, J. M.; Reijerse, E.; Lubitz, W.; Happe, T.; Artero, V.; Fontecave, M. Biomimetic Assembly and Activation of [FeFe]-hydrogenases. *Nature* **2013**, *499*, 66−69. (f) Utschig, L. M.; Silver, S. C.; Mulfort, K. L.; Tiede, D. M. Nature-driven Photochemistry for Catalytic Solar Hydrogen Production: a Photosystem I-transition Metal Catalyst Hybrid. *J. Am. Chem. Soc.* **2011**, *133*, 16334−16337.

(10) (a) Kandemir, B.; Chakraborty, S.; Guo, Y.; Bren, K. L. Semisynthetic and Biomolecular Hydrogen Evolution Catalysts. *Inorg. Chem.* **2016**, *55*, 467−477. (b) Slater, J. W.; Shafaat, H. S. Nickel-substituted Rubredoxin as a Minimal Enzyme Model for Hydrogenase. *J. Phys. Chem. Lett.* **2015**, *6*, 3731−3736. (c) Sommer, D. J.; Vaughn, M. D.; Clark, B. C.; Tomlin, J.; Roy, A.; Ghirlanda, G. Reengineering Cyt b for Hydrogen Production: A facile Route to Artificial Hydrogenases. *Biochim. Biophys. Acta, Bioenerg.* **2016**, *1857*, 598−603. (d) Sommer, D. J.; Vaughn, M. D.; Ghirlanda, G. Protein Secondary-shell Interactions Enhance the Photoinduced Hydrogen Production of Cobalt Protoporphyrin IX. *Chem. Commun.* **2014**, *50*, 15852−15855. (e) Kleingardner, J. G.; Kandemir, B.; Bren, K. L. Hydrogen Evolution from Neutral Water under Aerobic Conditions Catalyzed by Cobalt Microperoxidase-11. *J. Am. Chem. Soc.* **2014**, *136*, 4−7. (f) Saint-Martin, P.; Lespinat, P. A.; Fauque, G.; Berlier, Y.; Legall, J.; Moura, I.; Teixeira, M.; Xavier, A. V.; Moura, J. J. G. Hydrogen Production and Deuterium-proton Exchange Reactions Catalyzed by Desulfovibrio Nickel(II)-substituted Rubredoxins. *Proc. Natl. Acad. Sci. U. S. A.* **1988**, *85*, 9378−9380.

(11) Weber, P. C.; Ohlendorf, D. H.; Wendoloski, J. J.; Salemme, F. R. Structural Origins of High-affinity Biotin Binding to Streptavidin. *Science* **1989**, *243*, 85−88.

(12) Wilson, M. E.; Whitesides, G. M. Conversion of a Protein to a Homogeneous Asymmetric Hydrogenation Catalyst by Site-specific Modification with a Diphosphinerhodium(I) Moiety. *J. Am. Chem. Soc.* **1978**, *100*, 306−307.

(13) (a) Liang, A. D.; Serrano-Plana, J.; Peterson, R. L.; Ward, T. R. Artificial Metalloenzymes Based on the Biotin−Streptavidin Technology: Enzymatic Cascades and Directed Evolution. *Acc. Chem. Res.* **2019**, *52*, 585. (b) Schwizer, F.; Okamoto, Y.; Heinisch, T.; Gu, Y.; Pellizzoni, M. M.; Lebrun, V.; Reuter, R.; Kohler, V.; Lewis, J. C.; Ward, T. R. Artificial Metalloenzymes: Reaction Scope and Optimization Strategies. *Chem. Rev.* **2018**, *118*, 142−231. (c) Heinisch, T.; Ward, T. R. Artificial Metalloenzymes Based on the Biotin-Streptavidin Technology: Challenges and Opportunities. *Acc. Chem. Res.* **2016**, *49*, 1711−1721. (d) Chatterjee, A.; Mallin, H.; Klehr, J.; Vallapurackal, J.; Finke, A. D.; Vera, L.; Marsh, M.; Ward, T. R. An Enantioselective Artificial Suzukiase Based on the Biotin−streptavidin Technology. *Chem. Sci.* **2016**, *7*, 673−677. (e) Dundas, C. M.; Demonte, D.; Park, S. Streptavidin-biotin Technology: Improvements and Innovations in Chemical and Biological Applications. *Appl. Microbiol. Biotechnol.* **2013**, *97*, 9343−9353. (f) Ward, T. R. Artificial Metalloenzymes Based on the Biotin-Avidin Technology: Enantiose-lective Catalysis and Beyond. *Acc. Chem. Res.* **2011**, *44*, 47−57. (g) Letondor, C.; Ward, T. R. Artificial Metalloenzymes for Enantioselective Catalysis: Recent Advances. *ChemBioChem* **2006**, *7*, 1845−1852.

(14) Keller, S. G.; Probst, B.; Heinisch, T.; Alberto, R.; Ward, T. R. Photo-driven Hydrogen Evolution by an Artificial Hydrogenase Utilizing the Biotin-Streptavidin Technology. *Helv. Chim. Acta* **2018**, *101*, e1800036.

(15) (a) Call, A.; Codolà, Z.; Acuña-Parés, F.; Lloret-Fillol, J. Photo- and Electrocatalytic H₂ Production by New First-row Transition-metal Complexes Based on an Aminopyridine Pentadentate Ligand. *Chem. - Eur. J.* **2014**, *20*, 6171−6183. (b) Call, A.; Franco, F.; Kandoth, N.; Fernández, S.; González-Béjar, M.; Pérez-Prieto, J.; Luis, J. M.; Lloret-Fillol, J. Understanding Light-driven H₂ Evolution through the Electronic Tuning of Aminopyridine Cobalt Complexes. *Chem. Sci.* **2018**, *9*, 2609−2619.

(16) Skander, M.; Humbert, N.; Collot, J.; Gradinaru, J.; Klein, G.; Loosli, A.; Sauser, J.; Zocchi, A.; Gilardoni, F.; Ward, T. R. Artificial Metalloenzymes: (Strept)avidin as Host for Enantioselective Hydrogenation by Achiral Biotinylated Rhodium-diphosphine Complexes. *J. Am. Chem. Soc.* **2004**, *126*, 14411−14418.

(17) Wilson, M. E.; Nuzzo, R. G.; Whitesides, G. M. Bis(2-diphenylphosphinoethyl)amine. A flexible Synthesis of Functionalized Chelating Diphosphines. *J. Am. Chem. Soc.* **1978**, *100*, 2269−2270.

(18) (a) Planas, O.; Whiteoak, C. J.; Martin-Diaconescu, V.; Gamba, I.; Luis, J. M.; Parella, T.; Company, A.; Ribas, X. Isolation of Key Organometallic Aryl-Co(III) Intermediates in Cobalt-Catalyzed C(sp²)−H Functionalizations and New Insights into Alkyne Annulation Reaction Mechanisms. *J. Am. Chem. Soc.* **2016**, *138*, 14388−14397. (b) Planas, O.; Roldán-Gómez, S.; Martin-Diaconescu, V.; Luis, J. M.; Company, A.; Ribas, X. Mechanistic Insights into the S_N2-type Reactivity of Aryl-Co(III) Masked-carbenes for C−C Bond Forming Transformations. *Chem. Sci.* **2018**, *9*, 5736−5746. (c) Sarangi, R.; Cho, J.; Nam, W.; Solomon, E. I. XAS and DFT Investigation of Mononuclear Cobalt(III) Peroxo Complexes: Electronic Control of the Geometric Structure in CoO_2 versus NiO_2 Systems. *Inorg. Chem.* **2011**, *50*, 614−620. (d) Fujita, E.; Furenlid, L. R.; Renner, M. W. Direct XANES Evidence for Charge Transfer in Co−CO₂ Complexes. *J. Am. Chem. Soc.* **1997**, *119*, 4549−4550.

(19) Nishida, Y.; Ida, K.; Kida, S. Investigation on Low-spin Cobalt(II) Complexes.X. [1] An ESR Study on Six-coordinate Complexes. *Inorg. Chim. Acta* **1980**, *38*, 113−116.

(20) (a) The overpotential is defined as the difference between the applied potential and the thermodynamic potential for the reduction of protons at given conditions. The overpotential is defined as the difference between the applied potential and the thermodinamic potential for the reduction of protons at given conditions. (b) The thermodyinamic potential for the electrocatalytic water reduction to H₂ at given pH (SCE, 1 atm of H₂) is $E(pH) = -0.241$ V $- 0.059$ V $\times$ pH. The thermodynamic potential for the electrocatalytic water reduction to H₂ at given pH (SCE, 1 atm of H₂) is $E(pH) = -0.241$ V $- 0.059$ V $\times$ pH.

(21) (a) McCrory, C. C.; Uyeda, C.; Peters, J. C. Electrocatalytic Hydrogen Evolution in Acidic Water with Molecular Cobalt Tetraazamacrocycles. *J. Am. Chem. Soc.* **2012**, *134*, 3164−3170. (b) Sun, Y.; Bigi, J. P.; Piro, N. A.; Tang, M. L.; Long, J. R.; Chang, C. J. Molecular Cobalt Pentapyridine Catalysts for Generating Hydrogen from Water. *J. Am. Chem. Soc.* **2011**, *133*, 9212−9215. (c) McNamara, W. R.; Han, Z.; Yin, C.-J. M.; Brennessel, W. W.; Holland, P. L.; Eisenberg, R. Cobalt-dithiolene Complexes for the Photocatalytic and Electrocatalytic Reduction of Protons in Aqueous Solutions. *Proc. Natl. Acad. Sci. U. S. A.* **2012**, *109*, 15594−15599. (d) Abe, T.; Kaneko, M. pH-dependent Electrocatalysis for Proton Reduction by Bis(2,2′:6′,2″-terpyridine) Cobalt(II) Complex Embedded in Nafion® Membrane. *J. Mol. Catal. A: Chem.* **2001**, *169*, 177−183. (e) Slater, J. W.; Marguet, S. C.; Monaco, H. A.; Shafaat, H. S. Going beyond Structure: Nickel-Substituted Rubredoxin as a Mechanistic Model for the [NiFe] Hydrogenases. *J. Am. Chem. Soc.* **2018**, *140*, 10250−10262.

(22) (a) Slattery, S. J.; Blaho, J. K.; Lehnes, J.; Goldsby, K. A. pH-Dependent Metal-based Redox Couples as Models for Proton-coupled Electron Transfer Reactions. *Coord. Chem. Rev.* **1998**, *174*, 391−416. (b) Save'ant, J.-M. *Elements of Molecular and Biomolecular Electrochemistry: An Electrochemical Approach to Electron Transfer Chemistry*; Wiley-Interscience: Hoboken, NJ, 2006. (c) Horvath, S.; Fernandez, L. E.; Appel, A. M.; Hammes-Schiffer, S. pH-dependent Reduction Potentials and Proton-coupled Electron Transfer Mechanisms in Hydrogen-producing Nickel Molecular Electrocatalysts. *Inorg. Chem.* **2013**, *52*, 3643−3652.

(23) Anxolabéhère-Mallart, E.; Costentin, C.; Fournier, M.; Nowak, S.; Robert, M.; Saveant, J. M. Boron-capped Tris(glyoximato) Cobalt Clathrochelate as a Precursor for the Electrodeposition of Nanoparticles Catalyzing H_2 Evolution in Water. *J. Am. Chem. Soc.* **2012**, *134*, 6104−6107.

(24) Bigi, J. P.; Hanna, T. E.; Harman, W. H.; Chang, A.; Chang, C. J. Electrocatalytic Reduction of Protons to Hydrogen by a Water-compatible Cobalt Polypyridyl Platform. *Chem. Commun.* **2010**, *46*, 958−960.

(25) Léger, C.; Elliott, S. J.; Hoke, K. R.; Jeuken, L. J. C.; Jones, A. K.; Armstrong, F. A. Enzyme Electrokinetics: using Protein Film Voltammetry to Investigate Redox Enzymes and their Mechanisms. *Biochemistry* **2003**, *42*, 8653−8662.

(26) (a) Cline, E. D.; Adamson, S. E.; Bernhard, S. Homogeneous Catalytic System for Photoinduced Hydrogen Production Utilizing Iridium and Rhodium Complexes. *Inorg. Chem.* **2008**, *47*, 10378−10388. (b) Curtin, P. N.; Tinker, L. L.; Burgess, C. M.; Cline, E. D.; Bernhard, S. Structure-activity Correlations among Iridium(III) Photosensitizers in a Robust Water-reducing System. *Inorg. Chem.* **2009**, *48*, 10498−10506. (c) Hanss, D.; Freys, J. C.; Bernardinelli, G.; Wenger, O. S. Cyclometalated Iridium(III) Complexes as Photosensitizers for Long-range Electron Transfer: Occurrence of a Coulomb Barrier. *Eur. J. Inorg. Chem.* **2009**, *2009*, 4850−4859. (d) Ladouceur, S.; Fortin, D.; Zysman-Colman, E. Role of Substitution on the Photophysical Properties of 5,5′-diaryl-2,2′-bipyridine (bpy*) in $[Ir(ppy)_2(bpy*)]PF_6$ Complexes: a Combined Experimental and Theoretical Study. *Inorg. Chem.* **2010**, *49*, 5625−5641.

(27) Simond, M. R.; Ballerat-Busserolles, K.; Coulier, Y.; Rodier, L.; Coxam, J. Y. Dissociation Constants of Protonated Amines in Water at Temperatures from 293.15 to 343.15 K. *J. Solution Chem.* **2012**, *41*, 130−142.

(28) Natali, M. Elucidating the Key Role of pH on Light-Driven Hydrogen Evolution by a Molecular Cobalt Catalyst. *ACS Catal.* **2017**, *7*, 1330−1339.

(29) Han, Z.; McNamara, W. R.; Eum, M. S.; Holland, P. L.; Eisenberg, R. A nickel thiolate catalyst for the long-lived photocatalytic production of hydrogen in a noble-metal-free system. *Angew. Chem., Int. Ed.* **2012**, *51*, 1667−1670.

(30) (a) Stayton, P. S.; Freitag, S.; Klumb, L. A.; Chilkoti, A.; Chu, V.; Penzotti, J. E.; To, R.; Hyre, D.; Le Trong, I.; Lybrand, T. P.; Stenkamp, R. E. Streptavidin−biotin Binding Energetics. *Biomol. Eng.* **1999**, *16*, 39−44. (b) DeChancie, J.; Houk, K. N. The Origins of Femtomolar Protein-ligand Binding: Hydrogen-bond Cooperativity and Desolvation Energetics in the Biotin-(Strept)avidin Binding Site. *J. Am. Chem. Soc.* **2007**, *129*, 5419−5429. (c) The structure used was taken from the protein data bank (PDB); 1MK5.

(31) Schiller, T. L.; Keddie, D. J.; Blakey, I.; Fredericks, P. M. Surface-enhanced Raman Encoded Polymer Stabilized Gold Nanoparticles: Demonstration of Potential for Use in Bioassays. *Eur. Polym. J.* **2017**, *87*, 508−518.

(32) *Data collection with APEX II*, version v2013, 4-1; Bruker AXS Inc.: Madison, WI, 2007.

(33) *Data reduction with Bruker SAINT*, version V8.30c; Bruker AXS Inc.: Madison, WI, 2007.

(34) *SADABS*, V2012/1; Bruker AXS Inc.: Madison, WI, 2001.Blessing, R. H. An empirical correction for absorption anisotropy. *Acta Crystallogr.* 1995, *A51*, 33-38.

(35) TWINABS, Version 2012/1; Bruker AXS scaling for twinned crystals: Blessing, R. H. An empirical correction for absorption anisotropy. *Acta Crystallogr., Sect. A: Found. Crystallogr.* **1995**, *A51*, 33−38.

(36) SHELXT; V2014/4, 2014: Sheldrick, G. M. SHELXT-integrated space-group and crystal determination. *Acta Crystallogr., Sect. A: Found. Adv.* **2015**, *A71*, 3−8.

(37) SHELXle: Hübschle, C. B.; Sheldrick, G. M.; Dittrich, B. ShelXle: a Qt graphical user interface for SHELXL. *J. Appl. Crystallogr.* **2011**, *44*, 1281−1284.

(38) SHELXL; SHELXL-2014/7, 2014: Sheldrick, G. M. SHELXT-integrated space-group and crystal determination. *Acta Crystallogr., Sect. A: Found. Adv.* **2015**, *A71*, 3−8.

(39) Stoll, S.; Schweiger, A. EasySpin, a Comprehensive Software Package for Spectral Simulation and Analysis in EPR. *J. Magn. Reson.* **2006**, *178*, 42−55.

(40) (a) Newville, M. IFEFFIT: Interactive XAFS Analysis and FEFF Fitting. *J. Synchrotron Radiat.* **2001**, *8*, 322−324. (b) Ravel, B.; Newville, M. ATHENA, ARTEMIS, HEPHAESTUS: Data Analysis for X-ray Absorption Spectroscopy using IFEFFIT. *J. Synchrotron Radiat.* **2005**, *12*, 537−541.

(41) *Gaussian 09*, Revision E.01; Gaussian, Inc.: Wallingford, CT, 2009.

(42) (a) Becke, A. D. *J. Chem. Phys.* **1993**, *98*, 1372−1377. (b) Becke, A. D. *J. Chem. Phys.* **1993**, *98*, 5648. (c) Lee, C. T.; Yang, W. T.; Parr, R. G. *Phys. Rev. B: Condens. Matter Mater. Phys.* **1988**, *37*, 785.

(43) Marenich, A. V.; Cramer, C. J.; Truhlar, D. G. Universal Solvation Model Based on Solute Electron Density and on a Continuum Model of the Solvent Defined by the Bulk Dielectric Constant and Atomic Surface Tensions. *J. Phys. Chem. B* **2009**, *113*, 6378−6396.

(44) Grimme, S. Semiempirical GGA-type Density Functional Constructed with a Long-range Dispersion Correction. *J. Comput. Chem.* **2006**, *27*, 1787−1799.

(45) www.chemcraftprog.com.

(46) Case, D. A.; Darden, T. A.; Cheatham, T. E.; Simmerling, C. L.; Wang, J.; Duke, R. E.; Luo, R.; Crowley, M.; Walker, R. C.; Zhang, W.; Merz, K. M.; Wang, B.; Hayik, S.; Roitberg, A.; Seabra, G.; Kolossváry, I.; Wong, K. F.; Paesani, F.; Vanicek, J.; Wu, X.; Brozell, S. R.; Steinbrecher, T.; Gohlke, H.; Yang, L.; Tan, C.; Mongan, J.; Hornak, V.; Cui, G.; Mathews, D. H.; Seetin, M. G.; Sagui, C.; Babin, V.; Kollman, P. A. *AMBER 16*; University of California: San Francisco, CA, 2016.

(47) Wang, J.; Wolf, R. M.; Caldwell, J. W.; Kollman, P. A.; Case, D. A. Development and Testing of a General Amber Force Field. *J. Comput. Chem.* **2004**, *25*, 1157−1174.

(48) Hu, L.; Ryde, U. Comparison of Methods to Obtain Force-Field Parameters for Metal Sites. *J. Chem. Theory Comput.* **2011**, *7*, 2452−2463.

(49) Dolinsky, T. J.; Nielsen, J. E.; McCammon, J. A.; Baker, N. A. PDB2PQR: an Automated Pipeline for the Setup of Poisson-Boltzmann Electrostatics Calculations. *Nucleic Acids Res.* **2004**, *32*, W665−667.

(50) Jorgensen, W. L.; Chandrasekhar, J.; Madura, J. D.; Impey, R. W.; Klein, M. L. Comparison of Simple Potential Functions for Simulating Liquid Water. *J. Chem. Phys.* **1983**, *79*, 926−935.

(51) Wang, J.; Cieplak, P.; Kollman, P. A. How Well Does a Restrained ElectrostaticPotential (RESP) Model Perform in Calculating Conformational Energies of Organic and Biological Molecules? *J. Comput. Chem.* **2000**, *21*, 1049−1074.

(52) Darden, T.; York, D.; Pedersen, L. Particle mesh Ewald: An Nlog(N) Method for Ewald Sums in Large Systems. *J. Chem. Phys.* **1993**, *98*, 10089−10092.